Model-Based Fault Diagnosis of a Planetary Gear: A Novel Approach Using Transmission Error

Jungho Park, Jong Moon Ha, Hyunseok Oh, Byeng D. Youn, Joo-Ho Choi, and Nam Ho Kim

***Abstract*—Extensive prior studies aimed at the development of diagnostic methods for planetary gearboxes have mainly examined acceleration and acoustic emission signals. Recently, due to the relationship between gear mesh stiffness and transmission error (TE), TE-based techniques have emerged as a promising way to analyze dynamic behavior of spur and helical gears. However, to date, TE has not been used as a measure to detect faults in planetary gears. In this paper, we propose a new methodology for model-based fault diagnostics of planetary gears using TE signals. A lumped parametric model of planetary gear dynamics was built to extract simulated TE signals, while accounting for the planet phasing effect, which is a peculiar characteristic of the planetary gear. Next, gear dynamic analysis was performed using TE signals, and TE-based damage features were calculated from the processed TE signals to quantitatively represent health conditions. The procedures described aforesaid were then applied to a case study of a planetary gear in a wind turbine gear train. From the results, we conclude that TE signals can be used to detect the faults, while enhancing understanding of the complex dynamic behaviors of planetary gears.**

***Index Terms*—Condition monitoring, dynamic analysis, fault diagnosis, planetary gear, prognostics and health management.**

Acronyms and Abbreviations

AE	Acoustic emission.
FC	Frequency center.
FEA	Finite element analysis.
FM0	Figure-of-merit zero.
GMS	Gear mesh stiffness.
P2P	Peak-to-peak.
RMS	Root-mean-squares.
TE	Transmission error.
TSA	Time synchronous averaging.

Manuscript received October 1, 2015; revised March 28, 2016; accepted July 7, 2016. Date of publication August 30, 2016; date of current version November 29, 2016. This work was supported in part by the Technology Innovation Program (10050980, System Level Reliability Assessment and Improvement for New Growth Power Industry Equipment) funded by the Ministry of Trade, Industry & Energy (MI, Korea) and in part by a grant from the Institute of Advanced Machinery and Design at Seoul National University (SNU-IAMD). *(Corresponding authors: H. Oh and B. D. Youn.)* Associate Editor: S. Bae.

J. Park, J. M. Ha, H. Oh, and B. D. Youn are with the Department of Mechanical and Aerospace Engineering, Seoul National University, Seoul 08826, South Korea (e-mail: hihijung@snu.ac.kr; billyhjm@snu.ac.kr; hyunseok52@gmail.com; bdyoun@snu.ac.kr).

J.-H. Choi is with the Department of Aerospace & Mechanical Engineering, Korea Aerospace University, Goyang 10540, South Korea (e-mail: jhchoi@kau.ac.kr).

N. H. Kim is with the Department of Mechanical and Aerospace Engineering, University of Florida, Gainesville, FL 32611 USA (e-mail: nkim@ufl.edu).

Color versions of one or more of the figures in this paper are available online at http://ieeexplore.ieee.org.

Digital Object Identifier 10.1109/TR.2016.2590997

Notation

a_i	ith time data point.
f	Frequency of data.
f_j^g	Gear mesh frequency for its jth harmonic.
$\boldsymbol{F}$	External force vector.
k_{rp}	Time-varying GMS for the ring-planet meshes.
k_{sp}	Time-varying GMS for the sun-planet meshes.
$[K]$	Stiffness matrix.
l	Total number of harmonics of gear mesh frequency.
m	Total number of data samples.
$[M]$	Mass matrix.
p	Circular pitch.
$\boldsymbol{q}$	Displacement vector.
$\ddot{\boldsymbol{q}}$	Acceleration vector.
r_{s}, r_{p}, r_{r}	Pitch circle radii of sun, planet, and ring gears.
$s(\cdot)$	Amplitude of a frequency component.
$T_{\mathrm{rp}}^{(\mathrm{ref})}$	Number of teeth in contact for the ring-planet meshes after applying the phase difference at the reference planet gear.
$\tilde{T}_{\mathrm{rp}}^{(\mathrm{ref})}$	Number of teeth in contact for the ring-planet meshes before applying the phase difference at the reference planet gear.
$T_{\mathrm{sp}}^{(\mathrm{ref})}$	Number of teeth in contact for the sun-planet meshes at the reference planet gear.
x_{s}, x_{p}, x_{r}	Translational displacements of x-axis for sun, planet, and ring gears.
y_{s}, y_{p}, y_{r}	Translational displacements of y-axis for sun, planet, and ring gears.
z_{s}, z_{p}, z_{r}	Translational displacements of z-axis for sun, planet, and ring gears.
Z_{s}, Z_{p}, Z_{r}	Number of sun, planet, and ring gear teeth.
Δ_{rp}	Phase difference between ring-planet meshes.
Δ_{rs}	Phase difference between sun-planet and ring-planet meshes.
Δ_{sp}	Phase difference between sun-planet meshes.
α_{s}, α_{p}, α_{r}	Rotational displacements of x-axis for sun, planet, and ring gears.
β_{s}, β_{p}, β_{r}	Rotational displacements of y-axis for sun, planet, and ring gears.
γ_{s}, γ_{p}, γ_{r}	Rotational displacements of z-axis for sun, planet, and ring gears.
δ_{rs}	Difference of pitch points between ring-planet and sun-planet meshes.
θ_{m}	Rotational angle of one mesh for the planet gear.
μ	Mean.
σ	Standard deviation.
φ	Pressure angle.

ψ_n Circumferential angle of the nth planet counted in a counterclockwise manner and measured from the reference planet gear.

ω Helical angle.

I. Introduction

PLANETARY gears are widely used in many engineering applications, such as wind turbines and helicopter transmission systems. As multiple planet gears can share a load, a planetary gear has a unique advantage in systems, where the intensity of transmitted loads is extremely high. Therefore, planetary gears are usually exposed to severe loading conditions, which could lead to failures such as fatigue crack and pitting [1]. Unexpected failures of a gear may result in substantial economic losses and safety problems. Thus, fault detection and diagnosis for planetary gears has received significant attention in recent decades. Most currently available techniques were developed by analyzing data from either vibration sensors or acoustic emission (AE) transducers.

Vibration-based techniques are currently the most widely accepted methods for detecting faults in planetary gears because, as compared to AE-based techniques, they do not require expensive devices for measuring and processing signals. Numerous studies have been conducted to identify efficient methods for analyzing vibration signals for planetary gear diagnostics. Barszcz and Randall [2] developed a spectral kurtosis technique to detect tooth cracks in a planetary gear. This study demonstrated a technique that can detect a tooth crack long before the gear fails. Lei *et al.* [3] proposed diagnostic features, such as the root mean squares of filtered signals, and the normalized summation of positive amplitudes of the difference spectrum after considering the unique behavior of the planetary gear. The adaptive optimal kernel method was proposed to account for the transient characteristics of the fault detection of the planetary gear [4]. Although significant progress has been made, there remain limitations of vibration-based fault diagnostic methods. For example, environmental noise and mechanical resonance can easily disturb acceleration signals [5]. In addition, failure criteria in vibration-based methods rely on subjective engineering decisions, which lack physical reasoning for differentiating the severity of a fault [6].

AE-based techniques have also been developed for fault diagnostics of planetary gears. Energy-based diagnostics features, such as kurtosis and crest factor of residual signals performed well in detecting incipient faults in planetary gears [7]. To relieve the high cost in processing AE signals, the heterodyne technique was developed [6]. Several studies reported that AE signal-based methods are more sensitive to early fault detection in gear systems as compared to methods utilizing vibration signals [6], [8]–[10]. However, AE-based techniques require a higher sampling rate. Thus, they are expensive to implement. Additionally, AE transducers need to be located close to the signal sources due to unwanted attenuation and noise, which can limit the use of AE-based fault diagnosis techniques in actual field applications [9].

Recently, transmission error (TE) has been investigated to detect tooth faults in a gear system [11], [12]. TE is defined as the angular difference between the ideal position of the output shaft of a gear drive without deflections and the actual position of the output shaft [13]. The evaluation of gear mesh stiffness (GMS) relates the magnitude of TE to the severity of gear faults [14]–[16]. Prior works demonstrated that various faults can affect GMS and, eventually, TE [17], [18]. Taylor [11] processed TE signals of spur gears to extract features sensitive to faults. Taylor's study examined spur gears made of acrylonitrile butadiene styrene plastic; however, direct application of this study is limited because most spur gears are made of steel. Feki *et al.* [12] developed a three-dimensional dynamic gear model that simulates gear tooth pitting with GMS variations for helical gears. The authors showed the effectiveness of the gear model in detecting artificially injected faults of pitting. However, to the best of our knowledge, all of the previous studies only focused on either spur or helical gears. None of the prior work has studied a planetary gear, although planetary gears are widely used for power conversion in transportation and wind turbines. A planetary gear, which consists of sun, ring, multiple planet gears, and a carrier, is known to show complex dynamic behaviors due to the planet phasing effect. The planet phasing effect cannot be found in other gears like spur and helical gears. Therefore, it is challenging to develop a model-based fault diagnostics methodology for planetary gears using TE-based techniques. This underscores the need to analyze the dynamic behavior of TE generation in planetary gears, which in turn will enable development of an effective TE-based fault diagnostic method.

To address this gap, in this paper, we analyze the kinetics of a planetary gear system with a focus on determining their effect on GMS and, ultimately, on TE. The goal of the study described here is to develop an effective diagnostic method for planetary gears. The paper is organized as follows. Section II reviews the geometric characteristics of planetary gears and the effect of planet phasing. In Section III, we develop a dynamic model for analysis of planetary gears, while accounting for the phasing effect to the change of GMS, which is used as an input to calculate TE signals. Section IV verifies relevant features to monitor the condition of planetary gears. To demonstrate the effectiveness of the proposed diagnostic method, a case study is presented in Section V. This paper concludes with a summary and recommendations for future work.

II. Review of a Planetary Gear

A planetary gear shows unique behaviors that cannot be found in spur and helical gears. This section presents: 1) the geometric characteristics of the planetary gear; and 2) an overview of the planet phasing effect.

A. Geometric Characteristics

A planetary gear is a gear system that consists of three types of gears—a ring gear, a sun gear, and multiple planet gears—and a carrier on which the planet gears sit. As multiple planet gears rotate around the sun gear, the planet gears share the load that the

TABLE I
WORKING CONDITIONS OF A PLANETARY GEAR

	Sun	Ring	Planet	Speed	Direction
Condition 1	Stationary	Driving	Driven	Decrease	Same as input
Condition 2	Stationary	Driven	Driving	Increase	Same as input
Condition 3	Driving	Stationary	Driven	Decrease	Same as input
Condition 4	Driven	Stationary	Driving	Increase	Same as input
Condition 5	Driving	Driven	Stationary	Decrease	Reverse of input
Condition 6	Driven	Driving	Stationary	Increase	Reverse of input

system carries. In a planetary gear, ring, sun, and planet gears can perform either as a driving component, a driven gear, or a stationary supporter. Different working conditions of driving, driven, and stationary components are listed in Table I [19]. As the input speed to a planetary gear can be amplified positively or negatively depending on the gear ratio, TE should be calculated differently to correspond with each working condition of the planetary gear.

In a planetary gear, while the sun and the ring gears rotate around their fixed axes, the axes of planet gears rotate around the sun gear. The planet gears mesh with both the sun gear and the ring gear while rotating around the sun gear. Due to these characteristics, a planetary gear shows unique behaviors that are not observed in gearboxes with fixed axes. These unique characteristics include: 1) multiple planet meshing, 2) multiple and time-varying vibration transmission paths, 3) different frequency spectra from fixed axis gears (e.g., existence of sidebands in a healthy state), and 4) low operating speed due to the large gear ratio [20].

B. Planet Phasing Effect

Among the characteristics of the planetary gear described in Section II-A, multiple planet meshing has a significant impact on the dynamic behavior of planetary gears due to the planet phasing effect. The planet phasing effect was originally proposed as a design strategy that adjusts the number of teeth in contact between the sun-planet and ring-planet pairs in a planetary gear. This design strategy was empirically established to reduce the noise and vibration of the planetary gear [21]. Later, the effect of modifying the number of gear teeth on the reduction of unwanted vibration and noise was experimentally quantified [22]. Then, the mechanism defining how the planet phasing effect could reduce the noise and vibration was identified using the force relationship between multiple meshes [23]. In another study, the geometric characteristics of the planetary gear with the planet phasing effect were analyzed and the phase difference was calculated using the geometry of the planetary gear [24].

Without the planet phasing effect, the number of teeth in contact will be identical 1) among the ring-planet meshes, 2) among the sun-planet meshes, and 3) between ring-planet meshes and sun-planet meshes. In this condition, the meshes in contact between sun-planet meshes and ring-planet meshes are described as being "in-phase." Theoretically, the same amount of load will be equally distributed among the ring-planet and sun-planet meshes. On the other hand, an "out-of-phase" condition can occur when the number of teeth in contact varies. From the design point of view, the out-of-phase condition is desirable, because vibration and noise in gears can be efficiently suppressed in this condition [23].

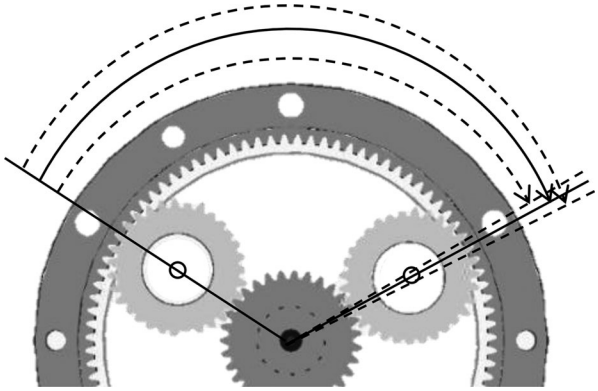

Fig. 1. Circumferential angles between the planet gears when the gears are distributed with the same contact conditions (i.e., in-phase state with dotted lines and arrows) and uniformly along the ring gear (i.e., out-of-phase with a solid line and arrow).

Fig. 1 shows the in-phase and out-of-phase states of the planetary gear. In the in-phase state, the planet gears have the same contact condition as indicated with dotted lines and arrows. When the planet gears are distributed uniformly along the ring gear, however, the planetary gear has an out-of-phase state, as indicated with the solid line and arrow. These phased contact conditions of gear teeth arising from the planet phasing effect lead to phased GMS behaviors in the planetary gear. This phased GMS results in different dynamic behaviors of a planetary gear from spur and helical gears. Therefore, it is essential to consider the planet phasing effect in understanding the dynamic behaviors of phased GMS and, ultimately, TE signals.

In Section II, we reviewed the characteristics of planetary gears for fault diagnostics using TE signals. Planetary gears show distinct behaviors compared to gears with fixed axes. In particular, the planet phasing effect causes complicated TE behaviors due to the out-of-phase state of the meshes in contact.

In the following section, a dynamic model for a planetary gear is constructed that considers the phasing effect to calculate credible TE signals for fault diagnostics.

III. PLANETARY GEAR MODELING TO SIMULATE TE SIGNALS

In this section, we develop a dynamic model of a planetary gear to reflect the changes of GMS arising from the planet phasing effect. First, the phasing effect is explained in terms of three types of phase differences. We then develop a dynamic model that incorporates the phase differences into the original planetary gear model. Finally, TE is evaluated from the modified dynamic model according to each working condition modeled for the planetary gear.

A. GMS Considering the Phasing Effect

In a planetary gear, we focus on three types of phase differences, specifically: 1) the phase difference between sun-planet

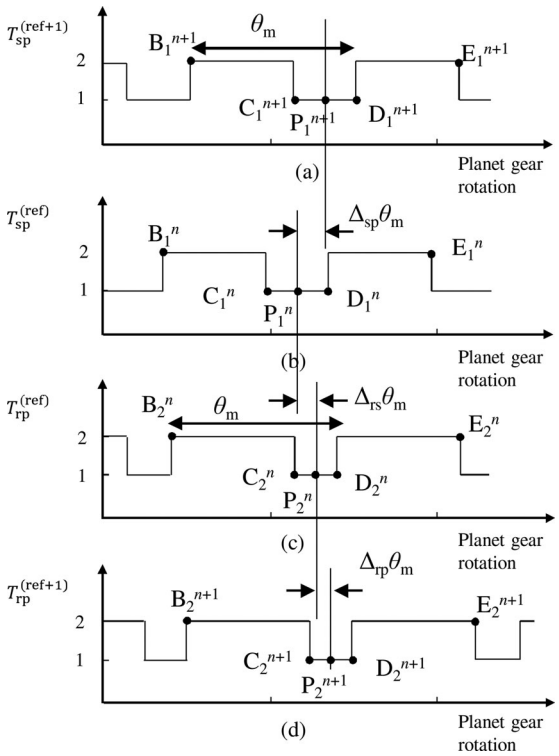

Fig. 2. Representative contact points in the sun-planet and ring-planet mesh with respect to planet gear rotation and the number of teeth in contact: the number of teeth in contact (a) with the sun-planet mesh for the reference planet, (b) with the sun in the sun-planet mesh for the first planet from the reference planet, (c) with the ring-planet mesh for the reference planet, and (d) with the ring-planet mesh for the first planet from the reference planet. Phase differences are illustrated between sun-planet meshes [(a) and (b)]; between sun-planet and ring-planet meshes [(b) and (c)]; and between ring-planet meshes [(c) and (d)].

meshes, 2) the phase difference between the sun-planet meshes and the ring-planet meshes, and 3) the phase difference between ring-planet meshes. As shown in Fig. 2, they correspond to $\Delta_{sp}\theta_m$, $\Delta_{rs}\theta_m$, and $\Delta_{rp}\theta_m$, respectively. In this section, we will briefly review how the three types of phase differences are derived, and then incorporate them into GMS.

1) Phase Differences between Sun-Planet Meshes: Phase differences exist between planet gears when they are meshing with a sun gear. The phase differences between sun-planet meshes ($=\Delta_{sp}$) are defined as [24]:

$$\Delta_{sp}=\begin{cases}(Z_s\psi_n)/2\pi, & \text{for clockwise planet rotation}\\ -(Z_s\psi_n)/2\pi, & \text{for counter-clockwise planet rotation}\end{cases} \tag{1}$$

where Z_s is the number of sun gear teeth and ψ_n is the circumferential angle of the nth planet counted in a counterclockwise manner and measured from the reference planet gear. The reference planet gear can be chosen randomly as the planet gears are uniformly distributed along the circumference of the ring gear.

To illustrate the phase difference between sun-planet meshes, as shown in Fig. 2, gear tooth contact starts at B, and ends at E. In between these points, there are C, D, and P that correspond to the beginning of single, double contact, and pitch point, respectively.

In Fig. 2(a) and (b), the phase differences are expressed with $\Delta_{sp}\theta_m$, where θ_m is the rotational angle of one mesh for the planet gear. The number of teeth in contact for the sun-planet meshes of the planet gear $T_{sp}^{(ref+1)}(\theta)$ adjacent to the reference planet gear is calculated by shifting that for the sun-planet meshes at the reference planet ($=T_{sp}^{(ref)}(\theta)$) as much as the phase difference between the sun-planet meshes ($=\Delta_{sp}$). The phase shift is performed based on each pitch point of the number of teeth in contact. Consequently, the relationship between the numbers of teeth in contact for adjacent sun-planet meshes can be expressed in the following equation:

$$T_{sp}^{(ref+1)}(\theta)=T_{sp}^{(ref)}(\theta-\Delta_{sp}\theta_m) \tag{2}$$

2) Phase Differences between Sun-Planet and Ring-Planet Meshes: The phase difference, Δ_{rs}, can be computed by investigating the geometry of the planetary gear. The basic concept used to calculate the phase difference is to estimate the difference of pitch points in the ring-planet and sun-planet meshes. As we can calculate the point when both ring-planet and sun-planet meshes are in their pitch points, the difference of the points implies the phase difference when it is converted into a fraction of the mesh period. A detailed explanation can be found in [24]. Therefore, Δ_{rs} is calculated as follows:

$$|\Delta_{rs}|=\delta_{rs}/p \tag{3}$$

where δ_{rs} is the difference of pitch points between ring-planet and sun-planet meshes, and p is the circular pitch. The sign of Δ_{rs} can be determined based on the contact sequence. Therefore, the relationship between the number of teeth in contact for the reference sun-planet and ring planet mesh is

$$T_{rp}^{(ref)}(\theta)=\tilde{T}_{rp}^{(ref)}(\theta-\Delta_{rs}\theta_m) \tag{4}$$

where $\tilde{T}_{rp}^{(ref)}$ and $T_{rp}^{(ref)}$ is the number of teeth in contact for the ring-planet mesh before and after applying the phase difference. The phase of $\tilde{T}_{rp}^{(ref)}$ is coincident with $T_{sp}^{(ref)}$. The phase difference can be applied as shown in Fig. 2(b) and (c).

3) Phase Differences between Ring-Planet Meshes: Phase differences between ring-planet meshes ($=\Delta_{rp}$) are similarly defined as follows:

$$\Delta_{rp}=\begin{cases}(Z_r\psi_n)/2\pi, & \text{for clockwise planet rotation}\\ -(Z_r\psi_n)/2\pi, & \text{for counter-clockwise planet rotation}\end{cases} \tag{5}$$

where Z_r is the number of ring gear teeth.

The same rule is applied to the number of teeth in contact with ring-planet meshes. The relationship between the number of teeth in contact for first ring-planet meshes from the reference planet ($=T_{rp}^{(ref+1)}(\theta)$) and reference ring-planet meshes ($=T_{rp}^{(ref)}(\theta)$) is expressed as follows:

$$T_{rp}^{(ref+1)}(\theta)=T_{rp}^{(ref)}(\theta-\Delta_{rp}\theta_m) \tag{6}$$

As shown in Fig. 2(c) and (d), the phase differences in terms of the fraction of the mesh period are expressed in $\Delta_{rp}\theta_m$.

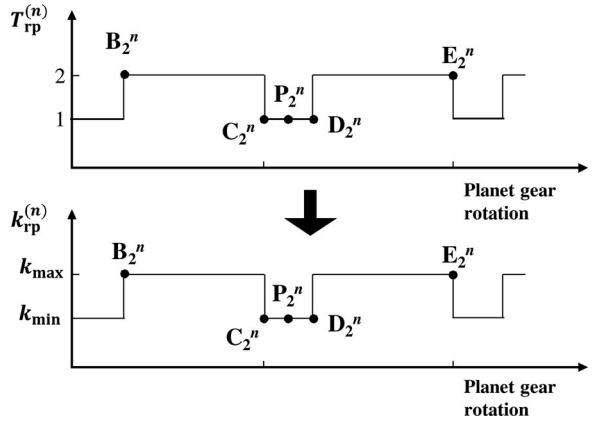

Fig. 3. Conversion from the number of teeth in contact ($= T_{rp}^{(n)}$) to GMS ($= k_{rp}^{(n)}$) for the nth ring-planet mesh.

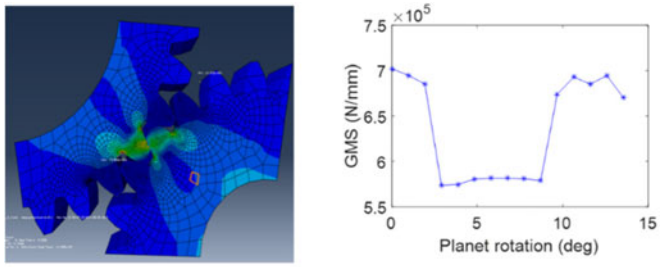

Fig. 4. Calculation of sun-planet GMS using (a) finite element analysis and (b) calculated values.

Many studies have shown that time-varying profiles of GMS at each tooth are subject to change due to variability of teeth, which include variations in things such as tip relief error and indexing error [25], [26]. In this study, however, we assumed that the variability between different teeth is negligible and the time-varying profiles of GMS are identical. Next, the number of teeth in contact with the sun-planet ($=T_{sp}(\theta)$) and ring-planet meshes ($=T_{rp}(\theta)$) can be converted into a time-varying profile of GMS (see Fig. 3) because GMS fluctuates along with the number of teeth in contact [27].

The points B, C, D, E, and P in Fig. 3 coincide with the ones in Fig. 2. Therefore, we can obtain the time-varying GMS for the ring-planet ($=k_{rp}(\theta)$) and sun-planet meshes ($=k_{sp}(\theta)$) by incorporating magnitudes of GMS and geometrical information, which are essential factors that affect dynamic behaviors of the gear. To obtain the magnitudes of GMS in one mesh cycle of each sun-planet and ring-planet mesh, finite element analysis (FEA) or analytic methods can be used. While an analytic method is preferred for shorter computation time, FEA is known to produce more accurate results despite their long computation time [18], [28]. For example, Fig. 4 shows the calculated profile of GMS for ring-planet mesh using FEA. When the calculated magnitudes of GMS are discretized as two values with maximum and minimum values, they can be converted into rectangular wave forms, like the one shown in Fig. 3.

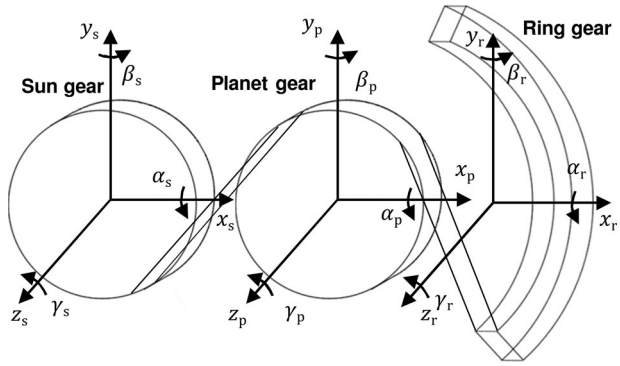

Fig. 5. Degrees of freedom for sun-planet and ring-planet gears.

B. Dynamic Model for a Planetary Gear

Dynamic models have been proposed by numerous studies to investigate the dynamic behaviors of the planetary gear [29]–[32]. In this study, we adopt a dynamic model for a planetary gear system originally proposed by Kim [32], and incorporate the phasing effect into the model. The magnitudes of GMS, k_{sp}, and k_{rp}, in the stiffness matrix of the previous model, are modified using GMS obtained from the phased number of teeth in contact.

Kim's model considered 12 degrees of freedom, including rotations and translations about x-, y-, z-axes for sun-planet and ring-planet relation. The model's equation of motion is

$$[M]\{\ddot{\boldsymbol{q}}\} - [K]\{\boldsymbol{q}\} = \{\boldsymbol{F}\} \tag{7}$$

where $[M]$ is the mass matrix; $\boldsymbol{q}$ is the displacement vector; $\ddot{\boldsymbol{q}}$ is the acceleration vector; $[K]$ is the stiffness matrix; and $\boldsymbol{F}$ is the external force vector. As shown in Fig. 5, the displacement vectors for sun-planet and planet-ring gears are (x_s, y_s, z_s, α_s, β_s, γ_s, x_p, y_p, z_p, α_p, β_p, γ_p) and (x_p, y_p, z_p, α_p, β_p, γ_p, x_r, y_r, z_r, α_r, β_r, γ_r), respectively. This model could consider the helix angle of gear teeth because it has 12 degrees of freedom and time-varying GMS can be included in stiffness components. The damping term can be ignored because the damping effect is not significant in characterizing the behavior of the planetary gear [33]. Among the aforesaid displacement vectors, this study focuses on the rotational displacements of the z-axis, γ_s, γ_p, and γ_r because we are focusing on the angular difference (i.e., TE).

The stiffness matrices for sun-planet and ring-planet gears used in this study are represented in Appendix. By incorporating the profiles of GMS obtained from the tooth contact condition into (A1) and (A2) in Appendix, the dynamic model for the planetary gear can be completed. The model has the 12 degrees of freedom. In this study, however, we only consider the rotating motion of the planetary gear.

C. TE in a Planetary Gear

TE can be calculated from the rotational displacements of the input shaft and the output shaft of the dynamic model. As various inputs and outputs can be obtained from the planetary gear of the same configuration, as mentioned in Section II-A, TE in a planetary gear also could be calculated differently in

Conditions 2, 4, and 6 using the rotational displacements of the z-axis outlined in Section III-B, as shown in the following [34]:

$$\mathrm{TE}=\begin{cases}\mathrm{TE}=\gamma_{\mathrm{r}}-\gamma_{\mathrm{c}}\cdot(Z_{\mathrm{r}}+Z_{\mathrm{s}})/Z_{\mathrm{r}}, & \text{for Condition 2}\\ \mathrm{TE}=\gamma_{\mathrm{s}}-\gamma_{\mathrm{c}}\cdot(Z_{\mathrm{r}}+Z_{\mathrm{s}})/Z_{\mathrm{s}}, & \text{for Condition 4}\\ \mathrm{TE}=\gamma_{\mathrm{s}}+\gamma_{\mathrm{r}}\cdot(Z_{\mathrm{r}}/Z_{\mathrm{s}}), & \text{for Condition 6.}\end{cases} \tag{8}$$

TE in Conditions 1, 3 and 5 can be calculated when input and output components are reversed from Conditions 2, 4 and 6. In Kim's modeling, however, the carrier motion is not considered. Therefore, we calculate the carrier rotation using planet rotation. It is defined as follows:

$$\gamma_{\mathrm{c}}=\gamma_{\mathrm{s}}+\gamma_{\mathrm{p}}\cdot Z_{\mathrm{p}}/(Z_{\mathrm{r}}-Z_{\mathrm{p}}) \tag{9}$$

where Z_{p} is the number of planet teeth, and γ_{c} is the rotational displacement of the carrier.

In this section, the profiles of GMS were calculated considering the planet mesh phasing that makes phase differences in each profile of GMS for the ring-planet mesh and the sun-planet mesh. Then, the dynamic model of a planetary gear was constructed with the phased profiles of GMS for the sun-planet and ring-planet gears. From the constructed dynamic model, we can calculate TE using the rotation of input and output motion while accounting for the planet mesh phasing. After calculating TE at each time step, the time series of TE should be quantitatively reshaped after signal processing techniques are performed for fault diagnostics.

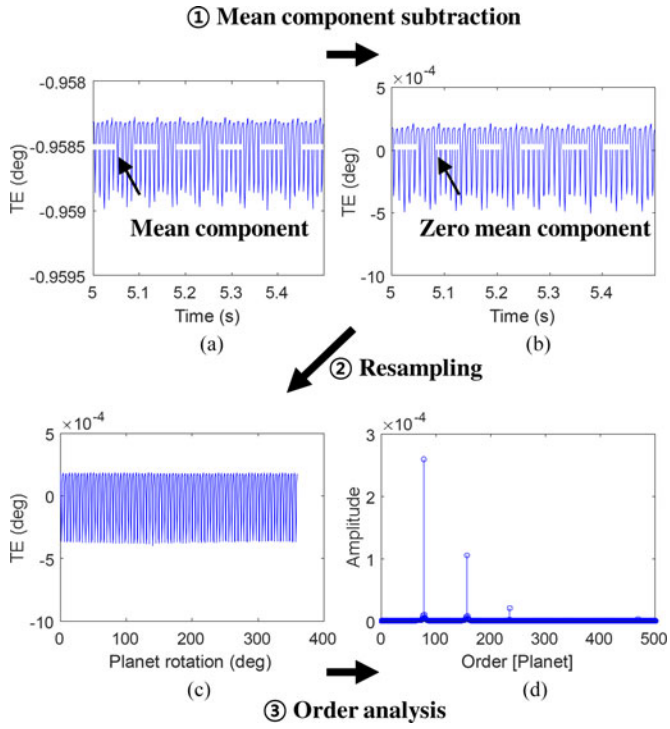

Fig. 6. Preprocessing procedures for TE signals: (a) raw TE signals, (b) mean-subtracted TE signals, (c) TSA signals resampled based on planet rotation, and (d) order analysis results.

IV. Feature Extraction for Detecting Faults With TE

TE generally shows periodic behaviors due to repeated shapes of GMS. In a planetary gear, TE is also affected by phase differences among the gears that come from multiple planet gears meshing with the sun and ring gears. This section explains preprocessing techniques that are used to alleviate the complexity of the peculiar TE signals in planetary gears. Then, TE-based features are extracted from the processed signals to classify the normal and abnormal states.

A. Preprocessing of TE

Fig. 6 shows the preprocessing procedures for TE signals that can be used to extract TE-based features. The procedures are made up of three steps that can reveal characteristic behaviors of the planetary gear in the time domain and the frequency domain. First, the offset from zero is subtracted from the TE signal. Due to deflection of the gear teeth, it is beneficial to subtract the mean component of the TE signal for sensitivity enhancement. Next, the shifted signals are resampled based on gear rotation, which is called angular resampling. In the resampling process, linear, bandwidth linear, and spline interpolation methods can be used [35]. After resampling, the effects of GMS on TE in the time domain can be easily identified as TE is represented in an angular domain. Also, the resampling can increase consistency in data. A noise reduction technique such as time synchronous averaging (TSA) can be used to further enhance the signal-to-noise ratio [36]. Last, frequency components of TE signals are analyzed using FFT. This procedure can identify the characteristic behavior in the frequency domain from multiple planet phasing effects. The frequency analysis may be performed before the resampling process. However, when the frequency analysis is performed after the resampling process, we can observe the frequency components per gear rotation, which enables order analysis and minimizes the effects of variable rotating speed.

B. TE-Based Feature Extraction

The TE-based features are extracted from the processed TE to quantify the health state of the system. In this study, root-mean-squares (RMS), kurtosis, frequency center (FC), and figure-of-merit zero (FM0) are used. Formulations of the features are listed in Table II.

In Table II, a_i is the ith time data point, m is the total number of data samples, μ is the mean of the data, σ is the standard deviation of the data, f is the frequency of the data, $s(f)$ is the amplitude of the frequency components, $P2P$ is the peak-to-peak (P2P) value of the data, f_j^g is gear mesh frequency and its jth harmonics, and l is the total number of harmonics. The first two are time-domain features, the third is a frequency-domain feature, and the last is a time-domain feature that uses frequency-domain information.

The RMS is well-known for quantifying the overall degradation degree of the system in the time domain [37], albeit insensitive to incipient failure. In this study, the RMS is adopted to evaluate relative sensitivity to faults through comparison with other features. The kurtosis measures the peakedness of a distribution with respect to normal distribution and the tail thickness [38]. Kurtosis is used to show degree of the TE signal's deviation from the mean value due to the fault of the gear. The

TABLE II
DEFINITION AND PHYSICAL INTERPRETATION OF TE-BASED FEATURES

	RMS	Kurtosis	FC	FM0
Definition	$\sqrt{\frac{1}{m}\sum_{i=1}^{m} a_i^2}$	$\frac{\sum_{i=1}^{m}[a_i-\mu]^4}{m\times(\sigma^2)^2}$	$\frac{\int_0^{+\infty} f\cdot s(f)df}{\int_0^{+\infty} s(f)df}$	$\frac{P2P}{\sum_{j=1}^{l} s(f_i^g)}$
Physical interpretation	Overall kinetic energy level	Deviating levels of signals with respect to normal distribution	Mean of the frequency components	Relative amplitude of peak-to-peak (P2P) values to meshing harmonics

TABLE III
SPECIFICATION OF THE PLANETARY GEAR IN A WIND TURBINE GEAR TRAIN USED IN THIS STUDY [38]

Gear data	Sun gear	Planet gear	Ring gear
Number of teeth	16	26	68
Pressure angle (degree)	24.6	24.6	24.6
Module (mm)	14.0	14.0	14.0
Pitch circle diameter (mm)	224	364	952
Root diameter (mm)	202	329	980
Transverse tooth thickness (mm)	25.0	18.5	25.0
Face width (mm)	180	180	180

FC calculates the mean of the frequency component and is used to observe the transition of the main frequency components. As gear faults are known to induce phase modulation [5], the FC can show how the faults affect the frequency components of the system. The FM0 is calculated by dividing the P2P value of the signals by the sum of the amplitude of the gear mesh frequency. The FM0 is known to detect localized faults in the measured signal [39]. The FM0 indicates the increase of magnitude of TE by calculating P2P values and the reduction in amplitude of the main frequency due to the fault signal.

V. CASE STUDY

This section presents a case study to demonstrate the effectiveness of TE for fault diagnostics using the techniques presented in Sections III and IV. The specifications of the planetary gear that we adopted in this study are shown in Table III [40]. Condition 4 (planet-driving and sun-driven) is used with the driving speed of 30 r/min and the applied torque of 180 kN · m. Additionally, we assumed a clockwise input, clockwise output, and a counterclockwise planet rotation. We adopted GMS results from a finite element analysis of an actual planetary gear train in a wind turbine. The finite element code developed by Vijayakar [41], [42] was used to calculate the time-varying GMS; its response was validated by other studies [23], [40], [43]. Given the above conditions, we obtained fault features using the TE calculated from the proposed dynamic model of the planetary gear considering the phasing effect.

A. Calculation of TE From the Dynamic Model of the Planetary Gear

TE of the planetary gear can be calculated by following the procedures described in Section III. To obtain time-varying GMS, the phase differences between sun-planet meshes ($=\Delta_{sp}$)

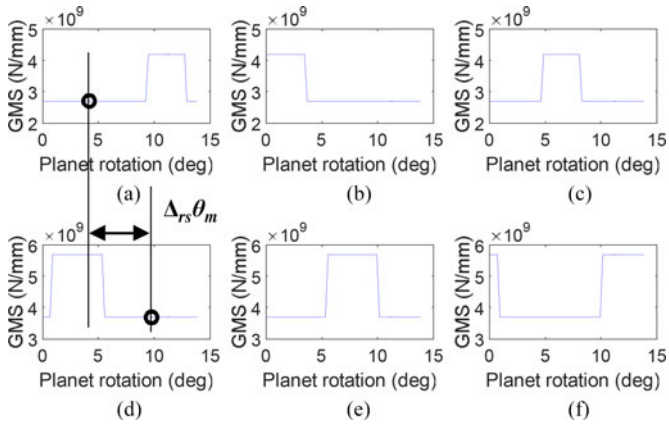

Fig. 7. GMS for one mesh of (a) first sun-planet gear, (b) second sun-planet gear, (c) third sun-planet gear, (d) first ring-planet gear, (e) second ring-planet gear, and (f) third ring-planet gear with phase differences considered.

and ring-planet meshes ($=\Delta_{rp}$) were calculated for a planetary gear with a counterclockwise planet rotation using (1) and (5), found in Section III-A. The calculated values of the phase differences were 68/3 and -16/3. They were converted into 2/3, as the phase differences are not affected by the integer component. From the previous study [40], the maximum and minimum magnitudes of GMS for the sun-planet mesh were determined to be 2.7×10^9 and 4.2×10^9 N/mm, respectively. Likewise, the maximum and minimum magnitudes of GMS for the ring-planet mesh are 3.7×10^9 and 5.7×10^9 N/mm, respectively. In Fig. 7(a)–(c), the profiles of GMS for sun-planet meshes are shown for one mesh with phase differences considered. Also, Fig. 7(d)–(f) shows the phased profiles of GMS for ring-planet meshes.

Next, the phase difference between the sun-planet and the ring-planet mesh ($=\Delta_{rs}$) was calculated using (3). The calculated absolute value is 0.625 and has a positive sign by the contact sequence. The calculated profiles of GMS during one mesh with the phase differences are shown in Fig. 7. The phase differences are considered between Fig. 7(a) and (d), Fig. 7(b) and (e), and Fig. 7(c) and (f).

For this study, we also parameterized time-varying profiles of GMS in a faulty state. The relationship between the profiles of GMS and gear faults has been investigated comprehensively [17], [18], [44]. Pandya and Parey [44] showed that a crack of 30% of a tooth's root induced about 10% decrease of GMS. In this research, we assumed three levels of faults resulting in 10%, 20%, and 30% decreases of the GMS. Although a crack fault

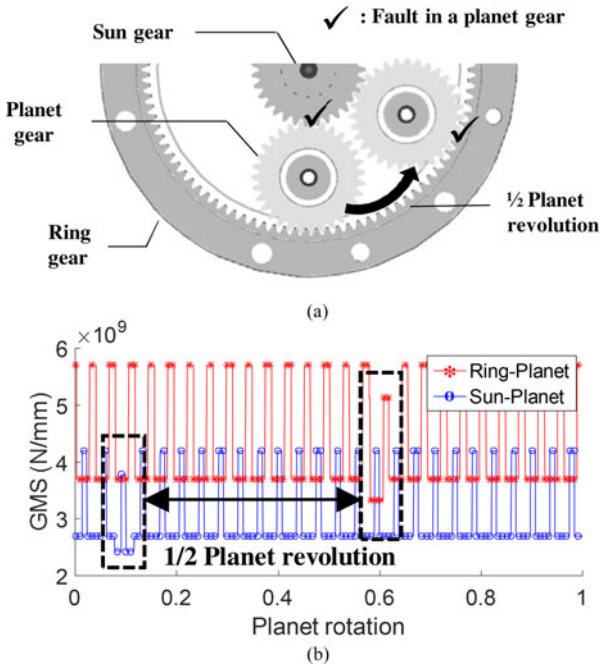

Fig. 8. (a) Illustration of the rotation of a faulty planet gear and (b) its influence on time-varying GMS of ring-planet and sun-planet meshes (indicated with dotted squares).

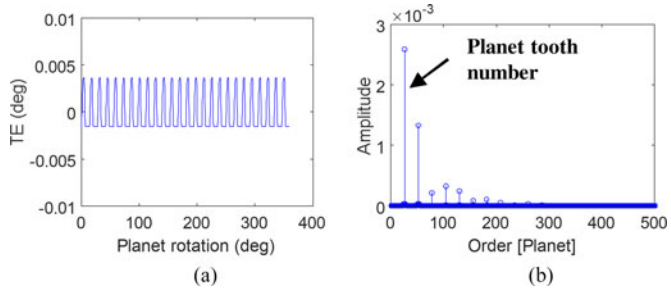

Fig. 9. TE of the planetary gear with an in-phase state: (a) resampled TE per one planet rotation and (b) the result of order analysis before incorporating the phasing effect.

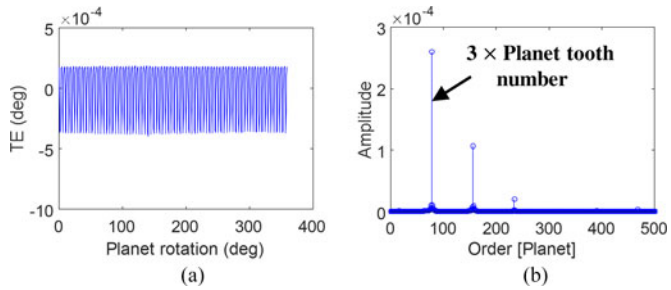

Fig. 10. TE of the planetary gear with an out-of-phase state: (a) resampled TE per one planet rotation and (b) the result of order analysis.

was considered in this case, faults like spalls and breakage are also known to induce the decreases of GMS [17]. It was revealed that the GMS shows different reduction behaviors under faults of spalls and cracks [45]. Therefore, it is possible to detect and differentiate the failure modes by monitoring the TE in gear systems. Consequently, the overall behaviors of TE from other types of faults are expected to be similar.

Also, we assumed that the faults exist in a planet gear. A faulty tooth in a planet gear would contact with both a sun and a ring gear repeatedly in a half-planet rotation. Therefore, the stiffness reductions appear with a phase difference equal to a half-planet rotation (like that shown in Fig. 8). In Fig. 8(b), the faulty tooth of the planet gear was parameterized by reducing the magnitudes of GMS in time-varying profiles of GMS. The phase difference of faulty time-varying GMS is a half-planet revolution.

Then, the time-varying profiles of GMS in normal and faulty gears were parameterized into a dynamic model, as described in Section III-B. As the planetary gear used in this study is a spur planetary gear, we ignored the translational displacements in the x- and y-axes, which are related to a helical angle. After inserting the geometrical values and working condition into (7), the TE of the planetary gear was calculated according to (8) with the Condition 4, as outlined in Section III-C.

B. Results of Processed TE

Using the signal processing techniques developed in Section IV-A, TE signals calculated in Section V-A were processed to effectively observe the behaviors of the gear in the time and frequency domains. Before analyzing the behaviors of TE from the planetary gear with the phasing effect, however, we first observed the behavior of TE before the phasing effect was incorporated. Fig. 9 shows the TE of the planetary gear with an in-phase state. Fig. 9(a) shows periodic behaviors of resampled TE per one planet rotation. Fig. 9(b) describes the result of order analysis of the TE signals. The frequency of the periodic motions in one planet rotation is the number of teeth of a planet gear (i.e., 26). The existence of the frequency was confirmed by the order analysis results, as shown in Fig. 9(b). Fig. 10 shows TE results when the phasing effect is incorporated. It was observed that the amplitudes became smaller compared to the case with the in-phase state. Also, the frequency of the periodic motion became higher, specifically 78. This increase happens from sequential meshing of planets due to planet mesh phasing. Without planet mesh phasing, the three planets would contact simultaneously with the ring and sun gears, and order analysis results would show harmonics of the planet tooth number like those shown in Fig. 9(b). However, as the phase differences from planet mesh phasing make the time difference planets contact with the ring and sun gears, the order analysis results show harmonics of three times the planet tooth number.

Fig. 11 shows TE results from the faulty planetary gears. TE from a faulty gear shows two different heights of sparks with a phase about 180°. These sparks happen due to a fault in the planet gear. As the planet gear with a fault rotates around the sun gear, the faulty tooth will contact with sun and ring gear repeatedly. Also, two different heights of sparks happen because the different magnitude of GMS for the ring-planet and sun-planet mesh induces a different reduction of GMS in each gear mesh. In order analysis results of a faulty gear, there appear low-frequency components and sidebands near the main

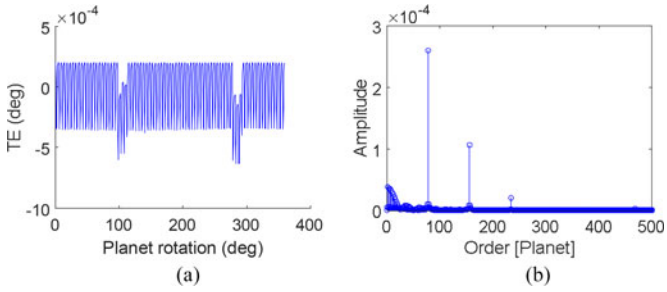

Fig. 11. TE of the faulty planetary gear with an out-of-phase state: (a) resampled TE per one planet rotation and (b) the result of order analysis.

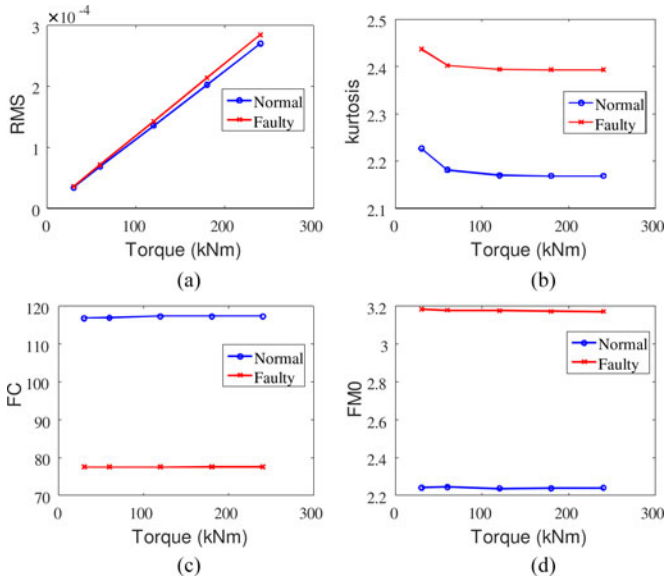

Fig. 12. (a) RMS, (b) kurtosis (c) FC and (d) FM0 values from a normal and faulty planetary gear at various torques (30, 60, 120, 180, 240 kN · m) with a driving speed of 30 r/min.

harmonics. These sidebands are due to two sparks of TE in the time-domain signal. This result is consistent with reports in the literature of studies using vibration signals and TE signals in a faulty gear [12], [17], [46].

C. Calculated Features in Various Operating Conditions

Four TE-based features described in Section IV-B were calculated using processed TE in various torques (30, 60, 120, 180, and 240 kN · m) and fault sizes (70%, 80%, and 90% of original magnitude of GMS). These calculations were performed to find out how the features change along the given operating conditions. For change of a torque, we investigated the robustness of the features in different operating conditions. As different magnitudes of torque are expected to change the amplitude of TE, we could notice how each feature behaves at varying conditions. For the change of magnitude of GMS, we could notice whether each feature could differentiate fault size. As different magnitudes of GMS imply different sizes of a tooth fault, we could, therefore, investigate the relationship between features and fault sizes. Figs. 12 and 13 show the calculated values of features at mentioned conditions.

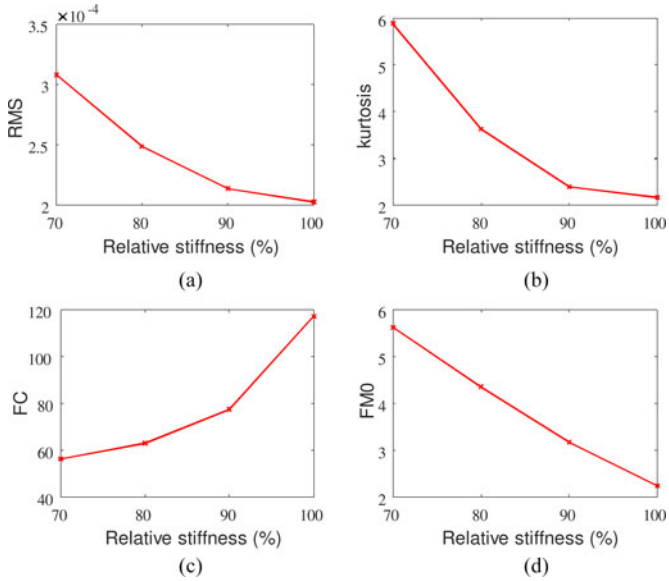

Fig. 13. (a) RMS, (b) kurtosis, (c) FC, and (d) FM0 values from calculated TE of different fault sizes.

First, we observed the behaviors of the features at torques of 30, 60, 120, 180, and 240 kN · m with a driving speed of 30 r/min. In the observation, 90% of GMS was chosen. In Fig. 12(a), RMS shows slightly higher value for a faulty case than a normal case. This result happens as the sparks in the TE take small portions of the integrated signals. The integration makes RMS more dependent on magnitude of torque, rather than existence of faults. For the kurtosis in Fig. 12(b), the tail of the TE distribution becomes thicker in a faulty case due to the sparked component of TE in the time domain, which causes a higher value of kurtosis. For the FC, the low-frequency components in Fig. 11(b) decrease the mean of the frequency component and make the FC value smaller. Therefore, classification between a normal and a faulty case is possible. An increase in P2P values from the spark at a faulty case makes the FM0 value larger; thus, we can discriminate between normal and faulty cases. Kurtosis, FM0, and FC are more sensitive at all torque levels than RMS for classification of the conditions between normal and abnormal. This result is because they are not calculated based on absolute magnitude of TE signals.

Also, the features were calculated at 70%, 80%, 90%, and 100% of normal GMS with a driving speed of 30 r/min and a torque of 180 kN · m. Fig. 13 shows that we can observe an increase of RMS, kurtosis, and FM0, and a decrease of FC. Larger faults make the sparks of TE larger, while other TE signals remain at their normal amplitude. This result makes RMS, kurtosis, and FM0 larger as a result of more severe faults. On the other hand, FC shows smaller values due to the magnified low-frequency components from the enlarged sparks. The results imply that the features calculated from processed TE could have the potential to differentiate fault levels at different operating conditions because 1) kurtosis, FM0, and FC in faulty states show distinct values from normal ones at different torque

magnitudes; and 2) these distinct values become severe as the fault sizes get bigger.

VI. Conclusion

This paper proposed model-based fault diagnostics for planetary gears using TE signals calculated from a dynamic model with phased GMS. This dynamic model for planetary gears was developed with a lumped parameter model. As the planet phasing effect was integrated into the model, GMS of the planetary gear was realistically calculated, which enabled credible calculation of TE signals in normal and faulty states. Using this information, we then identified the mesh phasing effect and faulty phase difference from the TE signals in the time and frequency domain. Next, the signals were processed, and four TE-based features—RMS, kurtosis, FC, and FM0—were calculated. We observed that kurtosis, FC, and FM0 performed more robustly across various torque and fault levels than was observed for RMS.

The main advantages of TE for fault diagnostics of a planetary gear are as follows. First, TE can help increase our understanding of the dynamic behaviors of the planetary gear. From the TE, we can observe the effect of planet phasing, which has a significant impact on the dynamic behavior of the gear. In the results of order analysis from the planet gear, order components of three times the planet tooth number appear due to sequential meshing of planet gears. Faulty phase difference of a half revolution arose in the TE signals due to meshing of the planet gear with the ring and sun gears. Moreover, it would be possible to infer the location of faults by observing the resampled TE signals. Second, TE has potential to detect incipient faults of gears and to differentiate fault levels. Vibration signals are known to react only to severe faults and cannot differentiate fault level. As TE is directly related to mesh stiffness, it can react sensitively with early faults. As gear faults like spalls and breakage are known to affect GMS, the signal could also react to incipient faults of different varieties. However, TE shows dependency on magnitude of torque, which could lead to difficulties in establishing the fault criteria. Therefore, it is recommended to calculate TE-based features based on relative magnitudes of TE, such as kurtosis, FM0, and FC, or to define different fault criteria for each operating condition.

In this study, dynamic behaviors of a planetary gear were investigated to develop a new fault diagnostics method using TE signals. However, the proposed methods are at this point limited to use in dynamic models of planetary gears and with simulated TE signals. Therefore, our future work will include application of the proposed diagnostic methods to measured TE data from testbeds. With the measured TE data, we plan to compare TE changes from the faults with those from the noise of operating variabilities. The GMS predicted by FEA will also be validated. Additionally, more advanced signal processing methods or TE-based features that can fully utilize characteristics of TE will be explored in future studies.

Appendix

The stiffness matrices for sun-planet and ring-planet gears are calculated using (A1) and (A2), where r_s, r_p, and r_r are the pitch circle radii of the sun, planet, and ring gears, respectively; φ is the pressure angle; and ω is the helical angle.

$$
[K] = k_{sp}\begin{bmatrix}
\sin^2\varphi & \frac{\sin 2\varphi}{2}\cos\omega & -\frac{\sin 2\varphi}{2}\sin\omega & 0 & r_s\frac{\sin 2\varphi}{2}\sin\omega & r_s\frac{\sin 2\varphi}{2}\cos\omega & -\sin^2\varphi & -\frac{\sin 2\varphi}{2}\cos\omega & \frac{\sin 2\varphi}{2}\sin\omega & 0 & r_p\frac{\sin 2\varphi}{2}\sin\omega & r_p\frac{\sin 2\varphi}{2}\cos\omega \\
 & \cos^2\varphi\cos^2\omega & -\cos^2\varphi\frac{\sin 2\omega}{2} & 0 & r_s\cos^2\varphi\frac{\sin 2\omega}{2} & r_s\cos^2\varphi\cos^2\omega & -\frac{\sin 2\varphi}{2}\cos\omega & -\cos^2\varphi\sin^2\omega & \cos^2\varphi\frac{\sin 2\omega}{2} & 0 & r_p\cos^2\varphi\frac{\sin 2\omega}{2} & r_p\cos^2\varphi\cos^2\omega \\
 & & \cos^2\varphi\sin^2\omega & 0 & -r_s\cos^2\varphi\sin^2\omega & -r_s\cos^2\varphi\frac{\sin 2\omega}{2} & \frac{\sin 2\varphi}{2}\sin\omega & \cos^2\varphi\frac{\sin 2\omega}{2} & -\cos^2\varphi\sin^2\omega & 0 & -r_p\cos^2\varphi\sin^2\omega & -r_p\cos^2\varphi\frac{\sin 2\omega}{2} \\
 & & & 0 & 0 & 0 & 0 & 0 & 0 & 0 & 0 & 0 \\
 & & & & r_s^2\cos^2\varphi\sin^2\omega & r_s^2\cos^2\varphi\frac{\sin 2\omega}{2} & -r_s\frac{\sin 2\varphi}{2}\sin\omega & -r_s\cos^2\varphi\frac{\sin 2\omega}{2} & r_s\cos^2\varphi\sin^2\omega & 0 & r_sr_p\cos^2\varphi\sin^2\omega & r_sr_p\cos^2\varphi\frac{\sin 2\omega}{2} \\
 & & & & & r_s^2\cos^2\varphi\cos^2\omega & -r_s\frac{\sin 2\varphi}{2}\cos\omega & -r_s\cos^2\varphi\cos^2\omega & r_s\cos^2\varphi\frac{\sin 2\omega}{2} & 0 & r_sr_p\cos^2\varphi\frac{\sin 2\omega}{2} & r_sr_p\cos^2\varphi\cos^2\omega \\
 & & & & & & \sin^2\varphi & \frac{\sin 2\varphi}{2}\cos\omega & -\frac{\sin 2\varphi}{2}\sin\omega & 0 & -r_p\frac{\sin 2\varphi}{2}\sin\omega & -r_p\frac{\sin 2\varphi}{2}\cos\omega \\
 & & & & & & & \cos^2\varphi\sin^2\omega & -\cos^2\varphi\frac{\sin 2\omega}{2} & 0 & r_p\cos^2\varphi\frac{\sin\omega}{2} & -r_p\cos^2\varphi\cos^2\omega \\
 & & & & & & & & \cos^2\varphi\cos^2\omega & 0 & r_p\cos^2\varphi\sin^2\omega & r_p\cos^2\varphi\frac{\sin 2\omega}{2} \\
 & & & & & & & & & 0 & 0 & 0 \\
 & & & & & & & & & & r_p^2\cos^2\varphi\sin^2\omega & r_p^2\cos^2\varphi\frac{\sin 2\omega}{2} \\
 & & & & & & & & & & & r_p^2\cos^2\varphi\cos^2\omega
\end{bmatrix} \tag{A1}
$$

$$
[K] = k_{rp}\begin{bmatrix}
\sin^2\varphi & -\frac{\sin 2\varphi}{2}\cos\omega & -\frac{\sin 2\varphi}{2}\sin\omega & 0 & r_p\frac{\sin 2\varphi}{2}\sin\omega & -r_p\frac{\sin 2\varphi}{2}\cos\omega & -\sin^2\varphi & \frac{\sin 2\varphi}{2}\cos\omega & \frac{\sin 2\varphi}{2}\sin\omega & 0 & -r_r\frac{\sin 2\varphi}{2}\sin\omega & r_r\frac{\sin 2\varphi}{2}\cos\omega \\
 & \cos^2\varphi\cos^2\omega & \cos^2\varphi\frac{\sin 2\omega}{2} & 0 & -r_p\cos^2\varphi\frac{\sin 2\omega}{2} & r_p\cos^2\varphi\cos^2\omega & \frac{\sin 2\varphi}{2}\cos\omega & -\cos^2\varphi\sin^2\omega & -\cos^2\varphi\frac{\sin 2\omega}{2} & 0 & r_r\cos^2\varphi\frac{\sin 2\omega}{2} & -r_r\cos^2\varphi\cos^2\omega \\
 & & \cos^2\varphi\sin^2\omega & 0 & -r_p\cos^2\varphi\sin^2\omega & r_p\cos^2\varphi\frac{\sin 2\omega}{2} & \frac{\sin 2\varphi}{2}\sin\omega & -\cos^2\varphi\frac{\sin 2\omega}{2} & -\cos^2\varphi\sin^2\omega & 0 & r_r\cos^2\varphi\sin^2\omega & -r_r\cos^2\varphi\frac{\sin 2\omega}{2} \\
 & & & 0 & 0 & 0 & 0 & 0 & 0 & 0 & 0 & 0 \\
 & & & & r_p^2\cos^2\varphi\sin^2\omega & -r_p^2\cos^2\varphi\frac{\sin 2\omega}{2} & -r_p\frac{\sin 2\varphi}{2}\sin\omega & r_p\cos^2\varphi\frac{\sin 2\omega}{2} & r_p\cos^2\varphi\sin^2\omega & 0 & -r_pr_r\cos^2\varphi\sin^2\omega & r_pr_r\cos^2\varphi\frac{\sin 2\omega}{2} \\
 & & & & & r_p^2\cos^2\varphi\cos^2\omega & r_p\frac{\sin 2\varphi}{2}\cos\omega & -r_p\cos^2\varphi\cos\omega & -r_p\cos^2\varphi\frac{\sin 2\omega}{2} & 0 & r_pr_r\cos^2\varphi\frac{\sin 2\omega}{2} & -r_pr_r\cos^2\varphi\cos^2\omega \\
 & & & & & & \sin^2\varphi & -\frac{\sin 2\varphi}{2}\cos\omega & -\frac{\sin 2\varphi}{2}\sin\omega & 0 & r_r\frac{\sin 2\varphi}{2}\sin\omega & -r_r\frac{\sin 2\varphi}{2}\cos\omega \\
 & & & & & & & \cos^2\varphi\cos^2\omega & \cos^2\varphi\frac{\sin 2\omega}{2} & 0 & -r_r\cos^2\varphi\frac{\sin 2\omega}{2} & r_r\cos^2\varphi\cos^2\omega \\
 & & & & & & & & \cos^2\varphi\sin^2\omega & 0 & -r_r\cos^2\varphi\sin^2\omega & r_r\cos^2\varphi\frac{\sin 2\omega}{2} \\
 & & & & & & & & & 0 & 0 & 0 \\
 & & & & & & & & & & r_r^2\cos^2\varphi\sin^2\omega & -r_r^2\cos^2\varphi\frac{\sin 2\omega}{2} \\
 & & & & & & & & & & & r_r^2\cos^2\varphi\cos^2\omega
\end{bmatrix} \tag{A2}
$$

sym

REFERENCES

[1] F. Chaari, T. Fakhfakh, and M. Haddar, "Dynamic analysis of a planetary gear failure caused by tooth pitting and cracking," *J. Failure Anal. Prevention*, vol. 6, pp. 73–78, 2006.

[2] T. Barszcz and R. B. Randall, "Application of spectral kurtosis for detection of a tooth crack in the planetary gear of a wind turbine," *Mech. Syst. Signal Process.*, vol. 23, pp. 1352–1365, 2009.

[3] Y. Lei, D. Kong, J. Lin, and M. J. Zuo, "Fault detection of planetary gearboxes using new diagnostic parameters," *Meas. Sci. Technol.*, vol. 23, p. 055605, 2012.

[4] Z. Feng and M. Liang, "Fault diagnosis of wind turbine planetary gearbox under nonstationary conditions via adaptive optimal kernel time–frequency analysis," *Renew. Energy*, vol. 66, pp. 468–477, 2014.

[5] X. Fan and M. J. Zuo, "Gearbox fault detection using Hilbert and wavelet packet transform," *Mech. Syst. Signal Process.*, vol. 20, pp. 966–982, 2006.

[6] Y. Qu, D. He, J. Yoon, B. Van Hecke, E. Bechhoefer, and J. Zhu, "Gearbox tooth cut fault diagnostics using acoustic emission and vibration sensors–a comparative study," *Sensors*, vol. 14, pp. 1372–1393, 2014.

[7] K. R. Al-Balushi and B. Samanta, "Gear fault diagnosis using energy-based features of acoustic emission signals," *Proc. Inst. Mech. Eng., Part I: J. Syst. Control Eng.*, vol. 216, pp. 249–263, 2002.

[8] T. H. Loutas, G. Sotiriades, I. Kalaitzoglou, and V. Kostopoulos, "Condition monitoring of a single-stage gearbox with artificially induced gear cracks utilizing on-line vibration and acoustic emission measurements," *Appl. Acoust.*, vol. 70, pp. 1148–1159, 2009.

[9] C. K. Tan, P. Irving, and D. Mba, "A comparative experimental study on the diagnostic and prognostic capabilities of acoustics emission, vibration and spectrometric oil analysis for spur gears," *Mech. Syst. Signal Process.*, vol. 21, pp. 208–233, 2007.

[10] F. Zhipeng, M. J. Zuo, H. Rujiang, C. Fulei, and M. El Badaoui, "Gear damage assessment based on cyclic spectral analysis," *IEEE Trans. Rel.*, vol. 60, no. 1, pp. 21–32, Mar. 2011.

[11] M. Taylor, "Gear fault detection using non-contact magnetic rotation position sensors," M.S. thesis, Dept. Mech. Mater. Eng,, Queen's Univ., Kingston, ON, Canada, 2010.

[12] J. C. Nabih Feki, Fabrice Ville and Philippe Velex, "Gear tooth pitting modelling and detection based on transmission error measurements," *Eur. J. Comput. Mech.*, vol. 22, pp. 106–119, 2013.

[13] D. Remond and J. Mahfoudh, "From transmission error measurements to angular sampling in rotating machines with discrete geometry," *Shock Vibration*, vol. 12, pp. 149–161, 2005.

[14] K. Mao, "An approach for powertrain gear transmission error prediction using the non-linear finite element method," *Proc. Inst. Mech. Eng., Part D: J. Automobile Eng.*, vol. 220, pp. 1455–1463, 2006.

[15] J. Wang and I. Howard, "Finite element analysis of high contact ratio spur gears in mesh," *J. Tribol.*, vol. 127, pp. 469–483, 2005.

[16] Z. Fuqiong, T. Zhigang, and Z. Yong, "Uncertainty quantification in gear remaining useful life prediction through an integrated prognostics method," *IEEE Trans. Rel.*, vol. 62, no. 1, pp. 146–159, Mar. 2013.

[17] F. Chaari, W. Baccar, M. S. Abbes, and M. Haddar, "Effect of spalling or tooth breakage on gearmesh stiffness and dynamic response of a one-stage spur gear transmission," *Eur. J. Mech.—A/Solids*, vol. 27, pp. 691–705, 2008.

[18] F. Chaari, T. Fakhfakh, and M. Haddar, "Analytical modelling of spur gear tooth crack and influence on gearmesh stiffness," *Eur. J. Mech.—A/Solids*, vol. 28, pp. 461–468, 2009.

[19] J. Erjavec and R. Thompson, *Automotive Technology: A Systems Approach*, 5th ed. Boston, MA, USA: Cengage Learning, 2014.

[20] Y. Lei, J. Lin, M. J. Zuo, and Z. He, "Condition monitoring and fault diagnosis of planetary gearboxes: A review," *Measurement*, vol. 48, pp. 292–305, 2014.

[21] R. G. Schlegel and K. C. Mard, "Transmission noise control—approached in helicopter design," in *Proc. ASME Des. Eng. Conf.*, New York, NY, USA, 1967, p. 55.

[22] R. L. Platt and R. D. Leopold, "A study on helical gear planetary phasing effects on transmission noise," *VDI-Ber.*, vol. 1230, pp. 793–807, 1996.

[23] R. G. Parker, "A physical explanation for the effectiveness of planet phasing to suppress planetary gear vibration," *J. Sound Vibration*, vol. 236, pp. 561–573, 2000.

[24] R. G. Parker and J. Lin, "Mesh phasing relationships in planetary and epicyclic gears," *J. Mech. Des.*, vol. 126, pp. 365–370, 2004.

[25] Z. Chen and Y. Shao, "Mesh stiffness calculation of a spur gear pair with tooth profile modification and tooth root crack," *Mechanism Mach. Theory*, vol. 62, pp. 63–74, 2013.

[26] M. Inalpolat, M. Handschuh, and A. Kahraman, "Influence of indexing errors on dynamic response of spur gear pairs," *Mech. Syst. Signal Process.*, vol. 60–61, pp. 391–405, 2015.

[27] Z. Chen and Y. Shao, "Dynamic simulation of planetary gear with tooth root crack in ring gear," *Eng. Failure Anal.*, vol. 31, pp. 8–18, 2013.

[28] Z. Fuqiong, T. Zhigang, E. Bechhoefer, and Z. Yong, "An integrated prognostics method under time-varying operating conditions," *IEEE Trans. Rel.*, vol. 64, no. 2, pp. 673–686, Jun. 2015.

[29] V. K. Ambarisha and R. G. Parker, "Nonlinear dynamics of planetary gears using analytical and finite element models," *J. Sound Vibration*, vol. 302, pp. 577–595, 2007.
[30] C.-J. Bahk and R. G. Parker, "Analytical solution for the nonlinear dynamics of planetary gears," *J. Comput. Nonlinear Dynam.*, vol. 6, p. 021007, 2011.
[31] Y. Guo and R. G. Parker, "Purely rotational model and vibration modes of compound planetary gears," *Mech. Mach. Theory*, vol. 45, pp. 365–377, 2010.
[32] J. Kim, "A study on the mesh stiffness of helical gear pair and dynamic characteristics of planetary gear train," Ph.D. dissertation, Dept. Mech. Eng., Seoul Nat. Univ., Seoul, South Korea, 2001.
[33] J. Lin and R. G. Parker, "Analytical characterization of the unique properties of planetary gear free vibration," *J. Vibration Acoustics*, vol. 121, pp. 316–321, 1999.
[34] R. J. Ferguson, "Short cuts for analyzing planetary gearing," *Mach. Des.*, vol. 55, pp. 55–58, 1983.
[35] E. Bechhoefer and M. Kingsley, "A review of time synchronous average algorithms," in *Proc. Annu. Conf. Prognostics Health Manage. Soc.*, San Diego, CA, USA, 2009, pp. 24–33.
[36] J. M. Ha, B. D. Youn, H. Oh, B. Han, Y. Jung, and J. Park, "Autocorrelation-based time synchronous averaging for condition monitoring of planetary gearboxes in wind turbines," *Mech. Syst. Signal Process.*, vol. 70, pp. 161–175, 2016.
[37] P. Večeř, M. Kreidl, and R. Šmíd, "Condition indicators for gearbox condition monitoring systems," *Acta Polytechnica*, vol. 45, no. 6, pp. 35–43, 2005.
[38] O. D. Mohammed, M. Rantatalo, and J.-O. Aidanpää, "Dynamic modelling of a one-stage spur gear system and vibration-based tooth crack detection analysis," *Mech. Syst. Signal Process.*, vol. 54–55, pp. 293–305, 2015.
[39] S. Choi and C. J. Li, "Estimation of gear tooth transverse crack size from vibration by fusing selected gear condition indices," *Meas. Sci. Technol.*, vol. 17, pp. 2395–2400, 2006.
[40] Y. Guo and R. G. Parker, "Dynamic modeling and analysis of a spur planetary gear involving tooth wedging and bearing clearance nonlinearity," *Eur. J. Mech.—A/Solids*, vol. 29, pp. 1022–1033, 2010.
[41] S. Vijayakar, "A combined surface integral and finite element solution for a three-dimensional contact problem," *Int. J. Numer. Methods Eng.*, vol. 31, pp. 525–545, 1991.
[42] S. Vijayakar. (2005). Calyx User's Manual. [Online]. Available: http://ansol.com
[43] A. Kahraman and S. Vijayakar, "Effect of internal gear flexibility on the quasi-static behavior of a planetary gear set," *J. Mech. Des.*, vol. 123, pp. 408–415, 2001.
[44] Y. Pandya and A. Parey, "Simulation of crack propagation in spur gear tooth for different gear parameter and its influence on mesh stiffness," *Eng. Failure Anal.*, vol. 30, pp. 124–137, 2013.
[45] J. Park, J. M. Ha, H. Oh, B. D. Youn, S. Park, and J.-H. Choi, "Experimental approach for estimating mesh stiffness in faulty states of rotating gear," in *Proc. Annu. Conf. Prognostics Health Manage. Soc.*, San Diego, CA, USA, 2015, pp. 618–624.
[46] Z. Cheng, N. Hu, and X. Zhang, "Crack level estimation approach for planetary gearbox based on simulation signal and GRA," *J. Sound Vibration*, vol. 331, pp. 5853–5863, 2012.

Jungho Park received the B.S. degree from Seoul National University, Seoul, South Korea, in 2012, where he is currently working toward the Ph.D. degree in the Department of Mechanical and Aerospace Engineering.

His research topic is prognostics and health management for gearboxes.

Mr. Park received two awards including the PHM Society Data Challenge Competition Winner in 2014 and 2015.

Jong Moon Ha received the B.S. degree from Hongik University, Seoul, South Korea, in 2011, and the M.S. degree from Seoul National University, Seoul, in 2013, where he is currently working toward the Ph.D. degree in the Department of Mechanical and Aerospace Engineering.

His research topic is prognostics and health management for gearboxes.

Mr. Ha received two international competition awards including the IEEE PHM Data Challenge Competition Winner in 2014 and the PHM Society Data Challenge Competition Winner in 2015.

Hyunseok Oh received the B.S. degree from Korea University, Seoul, South Korea, in 2004, the M.S. degree from KAIST, Daejeon, South Korea, in 2006, and the Ph.D. degree from the University of Maryland, College Park, MD, USA, in 2012, all in mechanical engineering.

He is currently a Research Professor in the Laboratory for System Health and Risk Management, Seoul National University, Seoul.

Dr. Oh received the A. James Clark Fellowship in 2007 and several awards including the IEEE PHM Data Challenge Competition Winner in 2012, and the PHM Society Data Challenge Competition Winner in 2014 and 2015.

Byeng D. Youn received the B.S. degree from Inha University, Incheon, South Korea, in 1996, the M.S. degree from KAIST, Daejeon, South Korea, in 1998, and the Ph.D. degree from the University of Iowa, Iowa City, IA, USA, in 2001, all in mechanical engineering.

He is currently an Associate Professor of mechanical and aerospace engineering at Seoul National University, Seoul, South Korea.

Dr. Youn's dedication and efforts in research have garnered substantive peer recognition resulting in notable awards including the ASME IDETC Best Paper Awards in 2001 and 2008, the ISSMO/Springer Prize for a Young Scientist in 2005, the IEEE PHM Competition Winner in 2014, and the PHM society Data Challenge Competition Winner in 2014 and 2015.

Joo-Ho Choi received the B.S. degree from Hanyang University, Seoul, South Korea, in 1981, and the M.S. and Ph.D. degrees from KAIST, Daejeon, South Korea, in 1983 and 1987, respectively, all in mechanical engineering.

During 1988–1996, he was with Samsung Corning as an Engineer for TV glasses development and production. In 1997, he joined the School of Aerospace and Mechanical Engineering, Korea Aerospace University, where he is currently a Professor. He has authored or coauthored more than 40 articles in peer-reviewed international journals. His research has focused on the statistical validation of computer model, and prognostics and health management (PHM).

Nam Ho Kim received the B.S. degree from Seoul National University, Seoul, South Korea, in 1989, the M.S. degree from KAIST, Daejeon, South Korea, in 1991, and the Ph.D. degree from the University of Iowa, Iowa City, IA, USA, in 1999, all in mechanical engineering.

He is currently a Professor and a Daniel C. Drucker Faculty Fellow of Mechanical and Aerospace Engineering, University of Florida, Gainesville, FL, USA.